TECHNICAL ARTICLE

Corrosion Behavior of Atmospheric Plasma-Sprayed YAG/8YSZ Double Ceramic-Layered Thermal Barrier Coatings in a Calcium–Magnesium–Alumino-Silicate Melt

Chunling Li, Bo Cheng ⓘ, Yi Zhang, Guosheng An, Yongjiang Sun, Yu Wang, and Wensheng Li

Calcium–magnesium–alumino-silicate (CMAS) corrosion is one of the important causes of failure in thermal barrier coatings (TBCs). Herein, 8YSZ ($8\%Y_2O_3$-ZrO_2) single and YAG ($Y_3Al_5O_{12}$)/8YSZ double ceramic-layered (DCL) TBCs were deposited on the Al_2O_3 substrate by atmospheric plasma spraying, respectively. The CMAS corrosion tests were conducted at 1250 °C for 1, 4, and 12 h, as well as on YAG/CMAS mixed powder (mass ratio 1:1) for 12 h. The microstructure and the corrosion products were analyzed to reveal the CMAS corrosion processes and mechanisms of these two types of TBCs. Results showed that YAG particle surface layer is slightly corroded by molten CMAS after 12 h at 1250 °C, which proved the good CMAS corrosion resistance and high-temperature stability of YAG. For the pure 8YSZ TBCs, the coating phase started to transfer from the as-sprayed tetrahedral phase to a monoclinic phase after corrosion for 1 h, and CMAS infiltrated the 8YSZ ceramic layer completely after 12 h. However, for the YAG/8YSZ DCL TBCs, only the high-melting-point apatite phase formed on the surface of TBCs blocked the further infiltration of CMAS by slowing further corrosion of CMAS. The protective apatite phase isolated CMAS from the internal YAG, keeping the bottom 8YSZ ceramic layer intact and extensively reducing the further damage to these TBCs.

1. Introduction

Thermal barrier coatings (TBCs) are widely used for the protection of hot-section components from high-temperature environments to improve the engine inlet temperature, thermal efficiency, and service lifetime (Ref 1-3). TBCs comprise a ceramic layer (top coating, TC), metal intermediate layer (bond coat, BC), and superalloy substrate (substrate, Sub). In service, mixed deposits (CaO-MgO-Al_2O_3-SiO_2, calcium–magnesium–alumino-silicate (CMAS)) arise in the natural environment (such as volcanic ash and gravel), anthropogenic activities (industrial smoke, dust, etc.); these are inhaled and attached to the surface of TBCs, which could cause the blockage of the holes for cooling film and the corrosion of TBCs, finally accelerating the failure of such TBCs (Ref 3). On the one hand, the CMAS adsorbed and deposited on the surface of the hot-end parts blocks the cooling holes on the surface of the gas film, which reduces the cooling effect and changes the temperature and stress fields of the components. On the other hand, molten CMAS penetrates the TBCs at high temperature, which accelerates the sintering and phase transition instability of the coating, resulting in a significant decrease in the service life and heat insulation performance of TBCs (Ref 4).

At present, 8YSZ ($8\% Y_2O_3$-ZrO_2) is the most widely used top-coating material and is prepared by the air plasma spraying (APS) or electron-beam physical vapor deposition (Ref 5-9). However, the limiting operating temperature of 8YSZ is about 1200 °C due to the potential phase transformation and severe sintering therein. Besides, that CMAS contaminating the 8YSZ top coating may also cause transformation of the t-ZrO_2 phase to an m-ZrO_2 phase (Ref 9-13). Therefore, the development of new CMAS-protective material has attracted more attention. Among the many new TBC candidate materials, pyrochlore, fluorite structure zirconate, and garnet structure substances ($Y_3Al_5O_{12}$, YAG) (Ref 14, 15) have attracted attention because of their excellent high-temperature mechanical properties and structural stability, good creep resistance (Ref 16), and low thermal conductivity (Ref 13-15). Besides, the oxygen diffusion rate of YAG ($10^{-20} m^2 s^{-1}$) (Ref 17) is about ten orders of magnitude lower than that of YSZ (10^{-10}-$10^{-11} m^2 s^{-1}$) (Ref 18, 19), which is conducive to blocking the transfer of oxygen to the bonding layer (Ref 20, 21). At the same time, when YAG is used together with YSZ, the high Y-content in YAG can inhibit the precipitation of Y_2O_3 stabilizer in YSZ and further improve its phase stability. Theoretically, from the

Chunling Li, State Key Laboratory of Advanced Processing and Recycling of Nonferrous Metals, School of Materials Science and Engineering, Lanzhou University of Technology, Lanzhou 730050 Gansu, China; and School of Mechanical and Electronical Engineering, Lanzhou University of Technology, Lanzhou 730050 Gansu, China; **Bo Cheng, Yi Zhang, Guosheng An, Yu Wang,** and **Wensheng Li**, State Key Laboratory of Advanced Processing and Recycling of Nonferrous Metals, School of Materials Science and Engineering, Lanzhou University of Technology, Lanzhou 730050 Gansu, China; and **Yongjiang Sun**, Gansu Luqiao Highway Investment Co., Ltd, Lanzhou 730050 Gansu, China. Contact e-mail: chengbo_o@126.com.

perspective of CMAS corrosion potentially causing the phase transformation of YSZ, combining the good mechanical properties of the YAG, YAG/YSZ double ceramic-layered (DCL) TBCs are expected to show better CMAS corrosion resistance, but the actual application of YAG/YSZ TBCs remains to be explored (Ref 22, 23).

In the present research, a YAG/8YSZ DCL TBC system structure was designed. The ceramic surface layer YAG could protect the bottom layer YSZ and may improve the CMAS corrosion resistance, endowing this DCL TBC system with better overall performance than its single ceramic counterpart (Ref 20). The authors found that for the YAG/8YSZ DCL TBCs, only the high melting point apatite phase formed on the surface of TBCs blocked the further infiltration of CMAS by sealing pores and cracks in the coating. The protective apatite phase isolated CMAS from the internal YAG kept the bottom 8YSZ ceramic layer intact and prevented further damage to the TBCs. This study aims to provide theoretical support for the application of YAG/8YSZ DCL TBCs in a CMAS corrosion environment.

2. Experiment

2.1 Materials and Preparation

YAG powders (12-40 μm, Xiamen Bajaxiang Microcrystalline Material Technology Co, China) and 204B-NS 8YSZ powders (35-86 μm, Oerlikon Metco, Switzerland) were used as ceramic layer materials. The raw YAG powder was agglomerated to improve the fluidity and morphology. The agglomeration process was described as follows: deionized water was used to prepare YAG powder suspension with a fixed content ratio of 50%, and after 1 h of ball milling, adding 3% polyvinyl alcohol, 1‰ dispersant, 1‰ defoamer (additive quality used to ensure the desired dry powder mass ratio) into the suspension and continuously ball-milled the material for 0.5 h; finally, the agglomerated YAG powder was obtained by LX-5 series centrifugal spray dryer. The particle size of YAG powder after agglomeration was 20-56 μm, realizing good fluidity and making it suitable for plasma spraying.

Based on the classical composition of CMAS (after neglecting trace amounts of NiO and other components), the chemical formula can be expressed as 33CaO-9MgO-13AlO$_{1.5}$-45SiO$_2$). In the present work, the CMAS powder was prepared as reported (Ref 21). The preparation process of CMAS powder was obtained by mixing and high-energy-ball milling the high-purity (99.99 %) oxides, dried at 70 °C and subjected to heat treatment at 1300 °C, before crushing and sieving. In this study, aluminum oxide with a similar composition to the TGO was selected as the substrate to prepare the DCL TBC, to avoid the effect of the possible superalloy oxidation products being

generated during the high-temperature corrosion process. The Al$_2$O$_3$ substrate measured φ20 mm $\times$ 5 mm.

2.2 Coating Preparation

Bond-coat-free TBC specimens were prepared to investigate the CMAS corrosion behavior and mechanism thereof. The surface of Al$_2$O$_3$ substrate was sand-blasted and cleaned before spraying. The surface ceramic layer was prepared by the APS system (GP-80, Jiujiang). The ceramic layer thickness of single 8YSZ was about 300 μm, and the thickness of 8YSZ and YAG was about 150 μm in this DCL YAG/8YSZ TBC system. The spraying parameters are listed in Table 1.

2.3 Corrosion Experiments and Phase Structure Analysis

The CMAS was uniformly coated with 12 mg/cm^2 on the surface of the cleaned single and DCL TBCs. The corrosion experiments were conducted by heating the specimens to 1250 °C at a rate of 10 °C/min in a resistance furnace, holding for 1, 4, and 12 h, respectively, and then cooling in furnace. In addition, the mixtures of CMAS and YAG powders at a mass ratio of 1:1 were treated by ball-milling and then heated as for the corrosion experiments (1250 °C for 12 h). A Quanta FEG 450 field emission scanning electron microscope (SEM) with EDS energy spectrum was used for observing microscopic morphology and micro-zone chemical composition analysis of YAG powders, 8YSZ, and YAG/8YSZ TBCs after CMAS corrosion. The phase structure analysis of the powder and coating surfaces was assessed using a D/MAX 2500PC x-ray diffractometer (XRD) with a scanning speed of 5°/min, a scanning range of 10-90°, an accelerating voltage of 40 kV and a current of 30 mA.

3. Results and Discussion

3.1 Corrosion Characteristics of YAG Powder and CMAS

Figure 1 shows the XRD patterns of CMAS and YAG mixed powder after 12 h at 1250 °C. The XRD peaks are still dominated by YAG peaks, accompanied by calcium feldspar (CaAl$_2$Si$_2$O$_8$) and apatite (Ca$_4$Y$_6$O(SiO$_4$)$_6$) peaks of lower intensity (Ref 22). The generation of apatite phase indicates the reaction between CMAS and YAG powder during high-temperature processing, while the generation of calcium feldspar phase may result from the reaction between CMAS and YAG powder or the self-crystallization of CMAS.

Figure 2 shows the morphology at microscopic-scale and EDS point sweep of CMAS and YAG mixed powders after holding at 1250 °C for 12 h. Figure 2(a) and (b) indicates that the CMAS corrosion medium adhered to the surface of YAG particles uniformly after high-temperature melting. The YAG particle matrix remains intact, the ball shape profile is clear, and

Table 1 Air plasma-spraying parameters

Parameters	Ar, L min^{-1}	H$_2$, L min^{-1}	Voltage, V	Current, A	Distance, mm	The gun traveling speed, mm min^{-1}	Number of passes	Total spraying duration, min	Powder feed rate, g min^{-1}
8YSZ	60	5.5	60	650	100	500	25	8	40
YAG	50	6.5	55	650	85	500	30	10	40

only a low degree of reaction occurs at the edge of the YAG powder particles, suggesting that YAG shows good high-temperature stability and CMAS corrosion resistance.

Figure 2(c), (d), and (e) shows the EDS point scan results of acicular substance A, massive substance B, and gray-black substance C (Fig. 2b), respectively: the compositions of substances A and B are similar, and it is considered that substance A and substance B are the reaction-generated acicular and massive apatite ($Ca_4Y_6O(SiO_4)_6$) by atomic ratio calculation (analysis of Fig. 1). The high-melting point inert apatite phase in the coating tends to hinder the penetration of CMAS and improve the CMAS corrosion resistance of the TBC system (Ref 23, 24). According to the EDS result at Point C, the calculated atomic ratio is about 1:2:2:10. Combined with the XRD analysis results in Fig. 1, due to the existence of measurement error, black substance C is speculated to be the structural product of calcium feldspar ($CaAl_2Si_2O_8$).
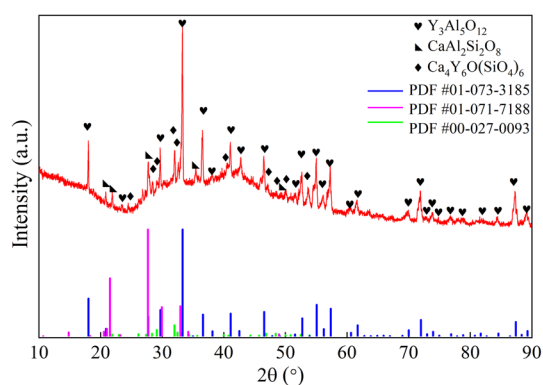

Fig. 1 XRD patterns of CMAS and YAG mixed powders after 12 h at 1250 °C

3.2 CMAS corrosion Product and Morphology Analysis

3.2.1 Surface Corrosion Morphology and Phase Analysis. Figure 3 shows the surface morphology of 8YSZ single ceramic (a-c) and YAG/8YSZ DCL TBCs (d-f) after corrosion for 1, 4, and 12 h, and EDS results (g-i). As shown in Fig. 3(a) and (d), the surfaces of single 8YSZ ceramic and DCL YAG/8YSZ TBCs remained smooth after 1 h of corrosion because the CMAS melted and adhered to the coating surface uniformly and did not penetrate after only that short a corrosion time. The surface morphology of 8YSZ single ceramic-layered TBCs after 4 and 12 h of CMAS corrosion is shown in Fig. 3(b) and (c): With the increase in corrosion time, gray island structures and black substances appear on the surface of 8YSZ TBCs and are then continuously transformed into small gray particles. For the DCL TBCs, there remains a layer of vitreous material adhered to the TBC surface even after 12 h of CMAS corrosion, and needles and lumps produced remained on the TBC surface. The rough surface of single ceramic-layered 8YSZ TBCs was probably caused by the strong reactivity of 8YSZ and molten CMAS; the relatively flat surface of YAG/YSZ TBCs may indicate their improved corrosion resistance.

Figure 3(g) shows the EDS results pertaining to point A in Fig. 3(c), which is ZrO_2 according to the calculated atomic proportions of Zr and O. The dark-gray substance B in Fig. 3(c) and the gray substance C are similar in composition and are speculated to be CMAS molten salts (Fig. 3h).

Figure 3(i) shows the point scan analysis of acicular substance D in Fig. 3(f): the composition is consistent with the composition and ratio of apatite ($Ca_4Y_6O(SiO_4)_6$, as shown in Fig. 2(c) found in the CMAS corrosion experiment on YAG powder.

Figure 4 demonstrates the XRD patterns of 8YSZ single ceramic (a) and YAG/8YSZ DCL (b) TBCs after corrosion. Figure 4(a) indicates that the monoclinic ZrO_2 peak emerges after 1 h of corrosion at 1250 °C, and a strong monoclinic ZrO_2 peak is found after 12 h of CMAS corrosion. It is believed that during the early stage of corrosion, CMAS molten salt did not
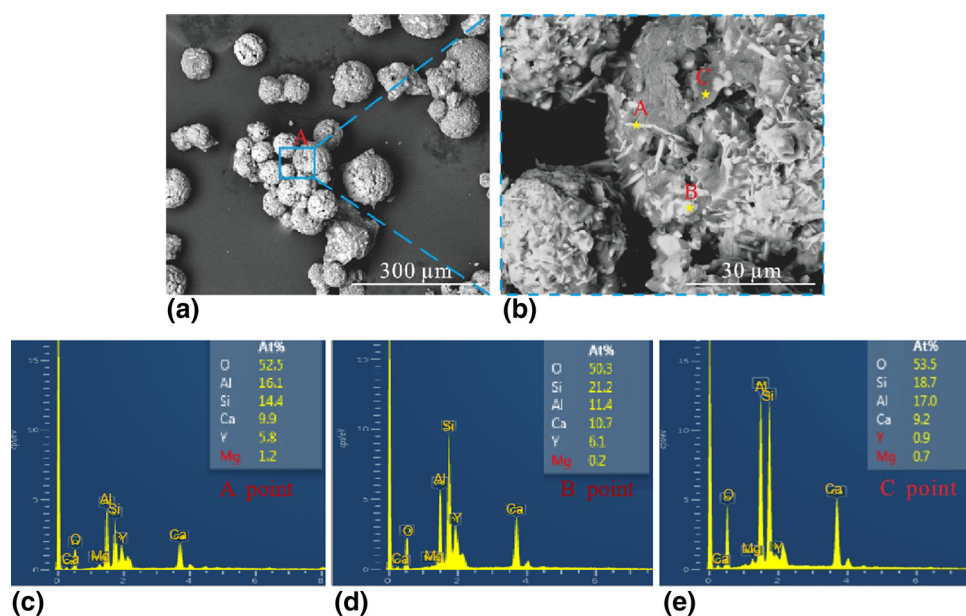

Fig. 2 Micro-morphology spot sweep pattern of CMAS and YAG mixed powder after 12 h at 1250 °C (a), (b), and EDS of CMAS and YAG mixed powder after 12 h at 1250 °C (c-e)
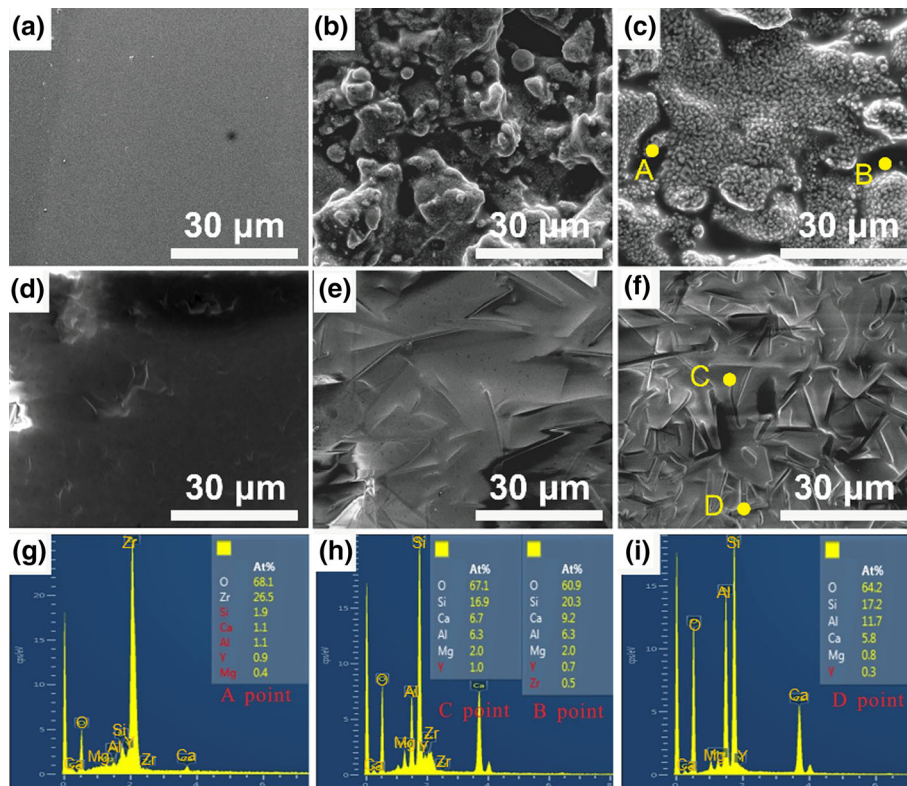
Fig. 3 Surface micro-morphology of 8YSZ single ceramics (a), (b), (c) and YAG/8YSZ double ceramics (d), (e), (f) TBCs after 1, 4 and 12 h corrosion and EDS results (g), (h) and (i)
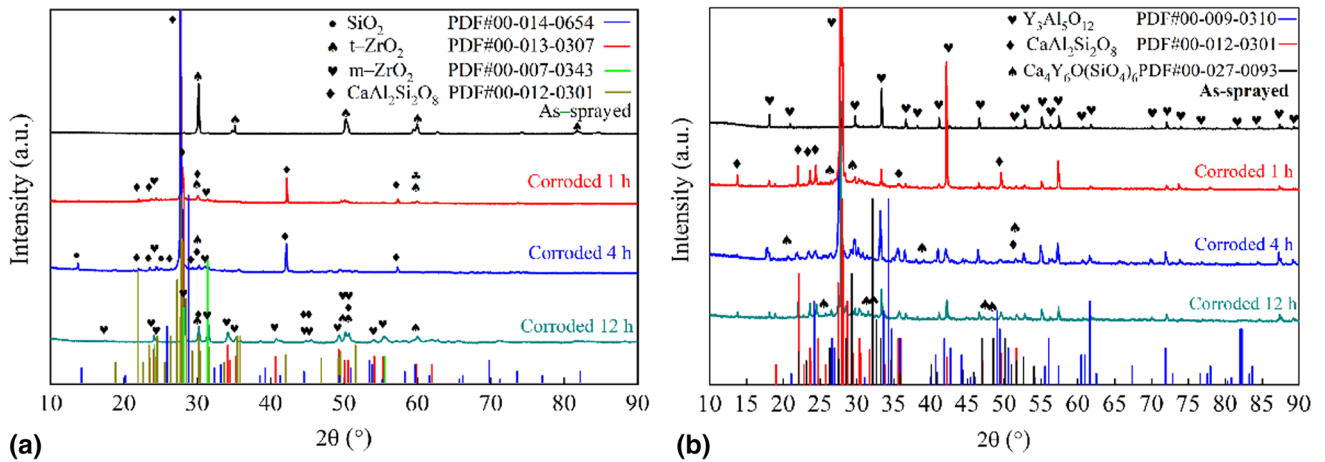

Fig. 4 XRD patterns of 8YSZ single ceramic (a) and YAG/8YSZ double ceramics (b) TBC corrosion surface

penetrate the TBCs. During corrosion, the molten CMAS triggered the transformation of 8YSZ from a metastable tetragonal phase to a monoclinic phase after 12 h of CMAS corrosion (Ref 25, 26). In (Ref 24), the same material system and preparation method were used herein (the cited research proved that 8YSZ underwent phase transformation only after sintering at 1300 °C for 200 h). Therefore, sintering alone was not the cause of phase transformation. The stronger ZrO_2 monoclinic peak after 12 h of CMAS corrosion also indicates that the reaction between 8YSZ and CMAS is more adequate, and there is no remaining molten CMAS to solidify and form a thicker vitreous layer on 8YSZ surface, which is consistent with the results of Fig. 3(b) and

(c) above. As shown in Fig. 4(b), the XRD results of the corrosion surface for YAG/8YSZ DCL TBCs are consistent with the results of surface morphology EDS analysis (Fig. 3g-i) and the analysis of the corroded physical phase results of YAG powder particles (Fig. 1), showing that apatite $(Ca_4Y_6O(SiO_4)_6)$ was the main corrosion product.

3.2.2 CMAS Corrosion Depth for YSZ and YAG/YSZ TBCs. Figure 5 shows the microscopic morphology of the cross sections of 8YSZ single ceramic-layered TBCs after CMAS corrosion at 1250 °C for 1 h (a-c), 4 h (d-f), and 12 h (g-i) at different magnifications. After CMAS corrosion for 1 h, CMAS began to penetrate the surface of the ceramic layer
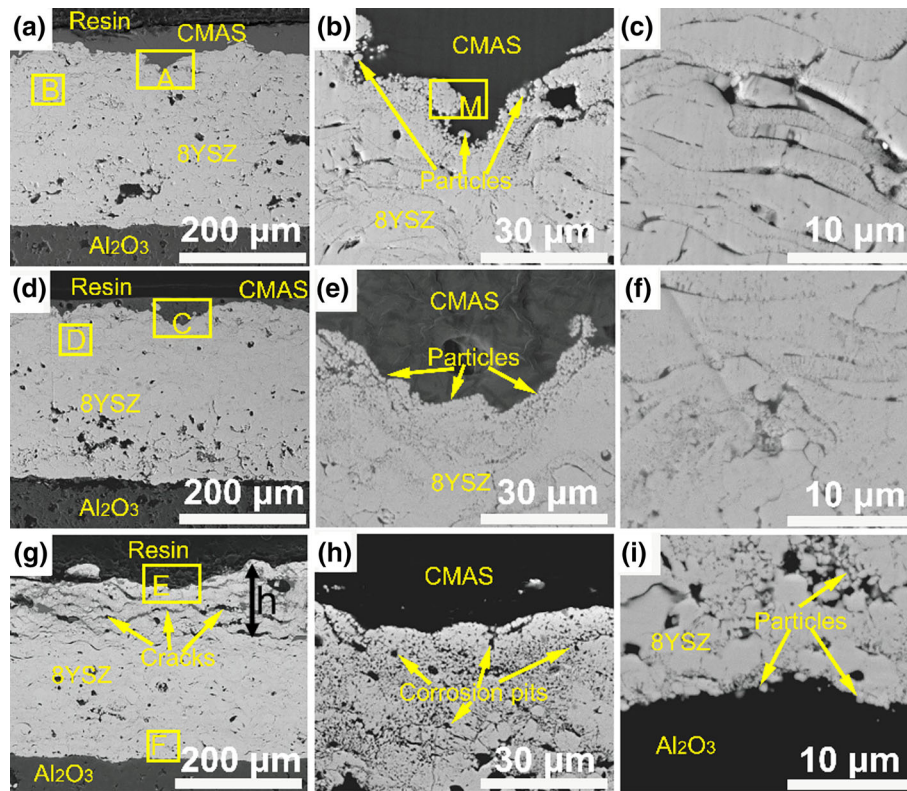
Fig. 5 8YSZ single ceramic-layered TBCs were corroded at 1250 °C for 1 h (a), (b) and (c), 4 h (d), (e) and (f), and 12 h (g), (h) and (i) cross-sectional micro-morphology

(Fig. 5b, area A in Fig. 5a and c), indicating that the ceramic layer maintains a typical layered structure. With the extension of corrosion time, obvious pitting corrosion characteristics appear in the surface area of the ceramic layer (Fig. 5e, area C in Fig. 5d). The lamellar structure of the ceramic layer in Fig. 5(f) is difficult to distinguish, which is presumed to be the interaction of high temperature and corrosion. Figure 5(g) illustrates that there are transverse large-scale cracks in the ceramic layer, forming a reticulated connection between tiny poles, with the entire ceramic layer being corroded (Fig. 5h and i). The corrosion depth (h in Fig. 5g) of the ceramic layer by CMAS is about 120 μm. It is reasonable to believe that the corrosion of CMAS accelerates the 8YSZ phase-transition process. The phase transformation of tetragonal phase to monoclinic phase accompanied by 3-5% volume change (Ref 27, 28) may contribute to the formation of large-scale cracks. It can be concluded that the conventional YSZ ceramic coating could not resist the attack of CMAS molten salt.

Figure 6 shows the microscopic morphology of the CMAS/8YSZ interface after CMAS corrosion of at 1250 °C for 1 h (high-magnification view of region M in Fig. 5b), where the EDS data pertaining to points *A*, *B*, and *C* are listed in Table. 2. Within the range of error in the energy spectrum, the dark substance A on the 8YSZ contains mainly Ca, Mg, Al, Si, and O, and the particles B and C are mainly composed of O and Zr. Combined with the analysis of Fig. 4(a), XRD pattern of the 8YSZ surface, it is concluded that the dark substance A is CMAS molten salt and the spherical particles B and C are ZrO_2 particles. This result is consistent with the results of Fig. 3(g) and (h) pertaining to the analysis of the spherical particles A and dark-gray substance B on the coating surface (Fig. 7).
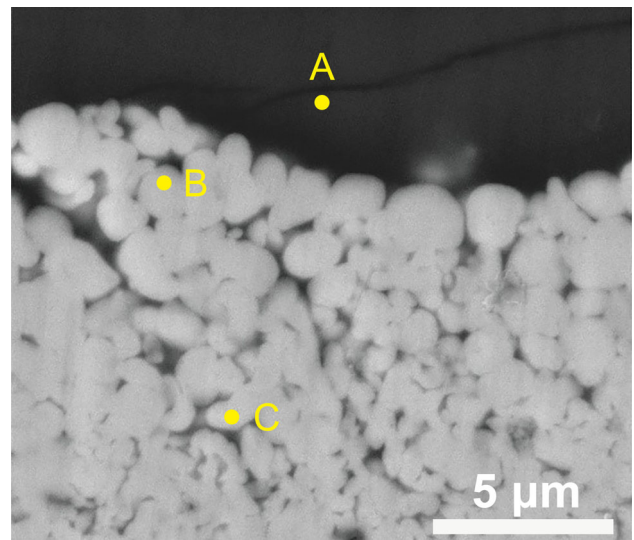

Fig. 6 CMAS/8YSZ interface morphology after 8YSZ single ceramic-layered TBCs were corroded at 1250 °C for 1 h

Figure 8 shows the cross sections of YAG/8YSZ DCL TBCs after CMAS corrosion at 1250 °C for 1 h (a-c), 4 h (d-f), and 12 h (g-i) at the same magnification. From the cross sections of YAG/8YSZ DCL TBCs after corrosion at 1250 °C for 1, 4, and 12 h (Fig. 8a, d, and g), a layer of dark-gray CMAS remained on the YAG surface, which is consistent with Fig. 3(d-f) showing the surface morphology of YAG/8YSZ DCL TBCs after corrosion for different times. This is consistent with the surface morphology of the YAG/8YSZ DCL ceramic TBCs

after corrosion for different times in Fig. 3(d-f). It is also observed that, during CMAS corrosion, molten salt penetrates the surface YAG ceramic layer, but the CMAS does not penetrate the whole YAG ceramic surface layer even after 12 h of CMAS corrosion. The underlying 8YSZ ceramic layer shows no obvious corrosion, and it is believed that YAG can protect the underlying ceramic layer 8YSZ from CMAS since no large-scale cracks were found.

Figure 8(b-h) shows magnified views of region A, C, and E in Fig. 8(a), (d), and (g), respectively. The YAG ceramic layer remains nearly intact and no CMAS corrosion behavior (no large-scale cracks) is visible, only a small amount of lumpy, acicular material is found at the CMAS/YAG interface. Figure 8(c), (f), and (i) shows high-magnification images of regions B, D, and F in Fig. 8(b), (d), and (g), respectively. The acicular and lumpy materials can be observed at the CMAS/YAG interface, and the amount thereof gradually increases with the increase in corrosion time. The EDS point analysis results in Fig. 8(i) are shown in Fig. 9 and Table 3.

The composition of point A is CMAS salt. The elemental composition of point B is similar to that of point C, which are speculated to be an apatite phase ($Ca_4Y_6O(SiO_4)_6$), combined with the surface XRD analysis in Fig. 4(b). This acicular,

Table 2 EDS point sweep data of 8YSZ single ceramic-layered TBCs corroded at 1250 °C for 1 h at the CMAS/8YSZ interface

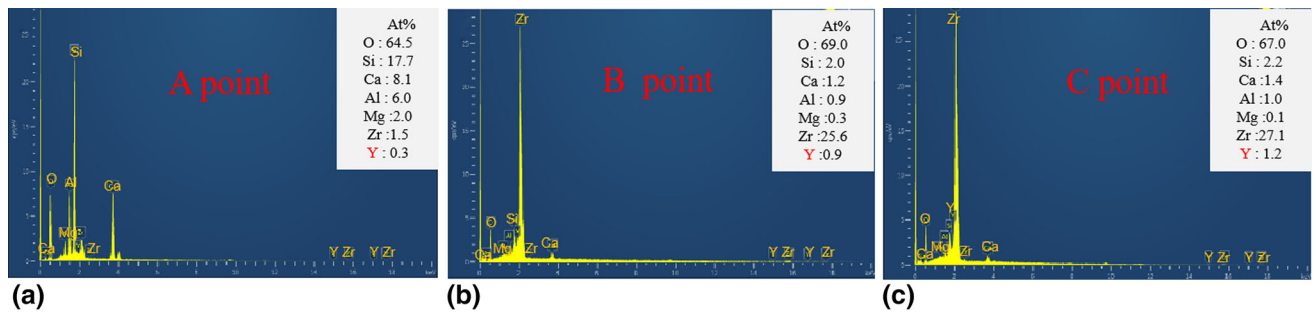| Element, at%	O	Si	Ca	Al	Mg	Zr	Y
A	64.5	17.7	8.1	6.0	2.0	1.5	0.3
B	69.0	2.0	1.2	0.9	0.3	25.6	0.9
C	67.0	2.2	1.4	1.0	0.1	27.1	1.2

Fig. 7 EDS of 8YSZ single ceramic-layered TBCs corroded at 1250 °C for 1 h at the CMAS/8YSZ interface (a), (b) and (c)
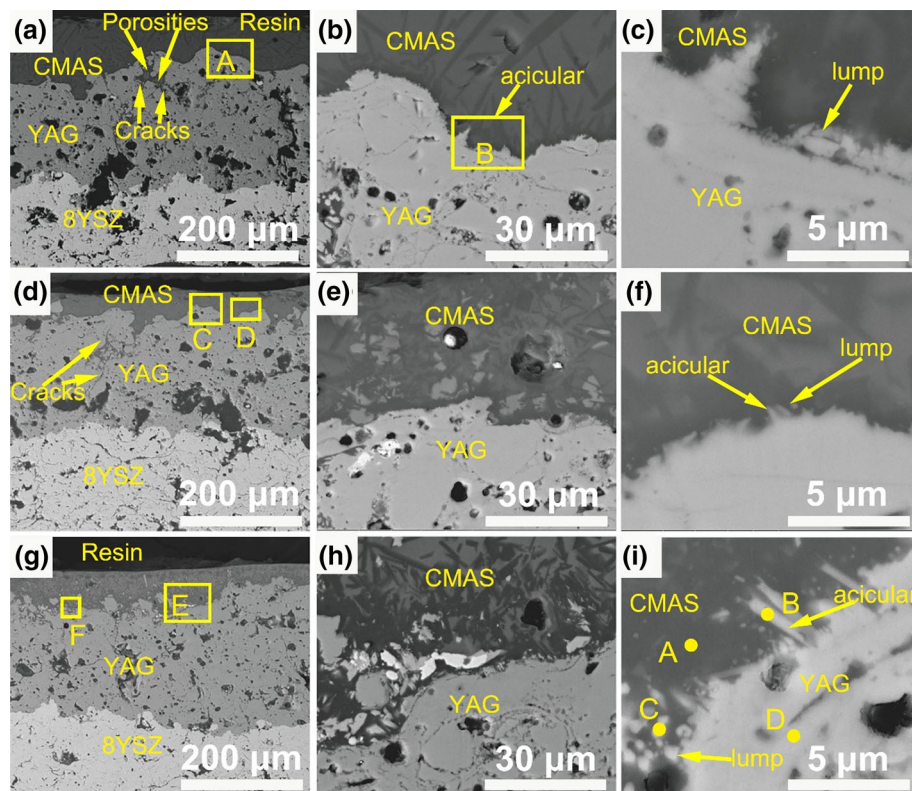

Fig. 8 YAG/8YSZ DCL TBCs were corroded at 1250 °C for 1 h (a), (b) and (c), 4 h (d), (e) and (f), and 12 h (g), (h) and (i) cross-sectional micro-morphology
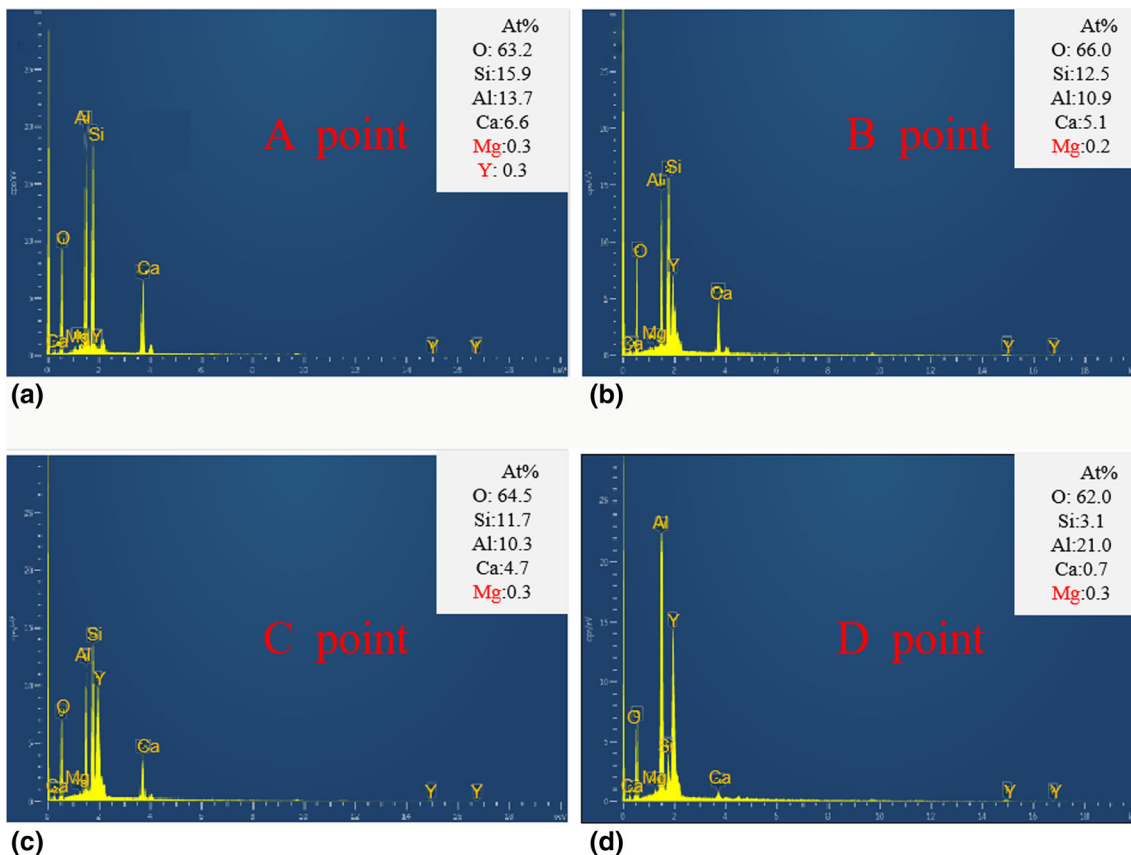
Fig. 9 EDS of points A to D in Fig. 7(i) (a-d)

Table 3 EDS point scan data of points A to D in Fig. 7(i)

Element, at%	O	Si	Al	Ca	Mg	Y
A	63.2	15.9	13.7	6.6	0.3	0.3
B	66.0	12.5	10.9	5.1	0.2	…
C	64.5	11.7	10.3	4.7	0.3	…
D	62.0	3.1	21.0	0.7	0.3	…

massive material is considered as an apatite mineral with the effect of slowing the CMAS corrosion process. Within the energy spectrum error range, point D is composed of mainly O, Al, and Y, which agrees with their proportions in the $Y_3Al_5O_{12}$ phase. This is confirmed to be YAG ($Y_3Al_5O_{12}$) when combined with the XRD data (Fig. 4b). Therefore, the reaction between YAG and CMAS only takes place at the contact interface, and the internal YAG structure remains intact. It is believed that the acicular corrosion products ($Ca_4Y_6O(SiO_4)_6$) can be attributed to the strong affinity of Y and Al in YAG to Ca and Si in CMAS, respectively. It is reported (Ref 29) that, when doping YAG with Ca and Si simultaneously (Ca^{2+} is exchanged with Y^{3+} while Si^{4+} is replaced with Al^{3+}), the overall defect reaction can be expressed using the following Kroger–Vink equation:

$$CaO + SiO_2 YAG Ca'_Y + Si^{\bullet}_{Al} + 3O^X_O \qquad (Eq\ 1)$$
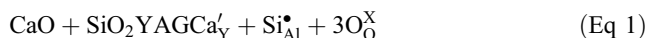
According to Eq 1, the Y^{3+} and Al^{3+} in YAG crystals at high temperature can be replaced by Ca^{2+} and Si^{4+} in CMAS,

respectively, and defective reactions occur to produce structural products such as calcium feldspar ($CaAl_2Si_2O_8$) and apatite ($Ca_4Y_6O(SiO_4)_6$). The appearance of such apatite with a higher melting point and excellent stability may be conducive to the improvement of CMAS corrosion resistance.

4. Conclusion

The CMAS corrosion behavior of two different structured TBCs was compared, and the reactivity between CMAS and YAG powders and CMAS corrosion behavior of APS-sprayed 8YSZ single ceramic-layered and YAG/8YSZ DCL TBC systems at 1250 °C were investigated. The conclusions are drawn as follows:

(1) YAG reacts with molten CMAS at 1250 °C for 12 h, but still shows good stability and CMAS corrosion resistance potential.
(2) YAG/8YSZ DCL TBCs show better CMAS corrosion resistance than that of 8YSZ single ceramic-layered TBCs, and the phase transition of 8YSZ induced by CMAS corrosion may be responsible for the failure of single ceramic-layered 8YSZ.
(3) The corrosion of YAG and CMAS is attributed to the strong affinity of Y and Al in YAG to Ca and Si in CMAS, and the corrosion products (such as calcium feldspar ($CaAl_2Si_2O_8$) and apatite ($Ca_4Y_6O(SiO_4)_6$))

show good stability in CMAS and slowed the corrosion and penetration of CMAS to YAG/8YSZ DCL TBCs

Acknowledgments

References

1. Q. Chen, P. Hu, and J. Pu, Interfacial Interaction and Roughness Parameters Effects on the Residual Stresses in DCL-TBC System with Different Thickness Distributions, *Ceram. Int.*, 2021, **47**(2), p 2781–2792.
2. A.C. Karaoglanli, K.M. Doleker, B. Demirel, A. Turk, and R. Varol, Effect of shot Peening on the Oxidation Behavior of Thermal Barrier Coatings, *Appl. Surf. Sci.*, 2015, **354**, p 314–322.
3. R. Darolia, Thermal Barrier Coatings Technology: Critical Review, Progress Update, Remaining Challenges and Prospects, *Int. Mater. Rev.*, 2013, **58**(6), p 315–348.
4. T. Steinke, D. Sebold, and D.E. Mack, A novel Test Approach for plasma-Sprayed Coatings Tested Simultaneously under CMAS and Thermal Gradient Cycling Conditions, *Surf. Coat. Tech.*, 2010, **205**(7), p 2287–2295.
5. A. Sharma, G. Witz, P.C. Howell, and N. Hitchman, Interplay of the Phase and the Chemical Composition of the Powder Feedstock on the Properties of Porous 8YSZ Thermal Barrier Coatings, *J. Eur. Ceram. Soc.*, 2020, **41**, p 3706–3716.
6. L.Y. Chen, X.X. Tian, and H.Y. Wang, Phase Interaction Induced Texture in a Plasma Sprayed-Remelted NiCrBSi Coating during Solidification: An Electron Backscatter Diffraction Study, *Surf. Coat. Tech.*, 2019, **358**, p 467–480.
7. J.J. Gomezchavez, R. Naraparaju, and C. Mikulla, Comparative Study of EB-PVD Gadolinium-Zirconate and Yttria-Rich Zirconia Coatings Performance against Fe-Containing Calcium-Magnesium-Aluminosilicate (CMAS) Infiltration, *Corros. Sci.*, 2021, **190**, p 190660.
8. P. Sang, L.Y. Chen, and C. Zhao, Particle Size-Dependent Microstructure, Hardness and Electrochemical Corrosion Behavior of Atmospheric Plasma Sprayed NiCrBSi Coatings, *Metals*, 2019, **9**(12), p 1342.
9. Y. Ozgurluk, A.C. Karaoglan, and H. Ahlatci, Comparison of Calcium-Magnesium-Alumina-Silicate (CMAS) Resistance Behavior of Produced with Electron Beam Physical Vapor Deposition (EB-PVD) Method YSZ and $Gd_2Zr_2O_7$/YSZ Thermal Barrier Coatings Systems, *Vacuum*, 2021, **194**, p 110576.
10. W. Fan, X. Song, and Y. Huang, Structure Change and Phase Transition Distribution Caused by CMAS Corrosion of YSZ Coating, *J. Inorg. Mater.*, 2021, **36**(10), p 1059.
11. A. Aygun, A.L. Vasiliev, N.P. Padture, and X. Ma, Novel Thermal Barrier Coatings that are Resistant to High-Temperature Attack by Glassy Deposits, *Acta. Mater.*, 2007, **55**(20), p 6734–6745.
12. H. Fang, W. Wang, J. Huang, and D. Ye, Investigation of CMAS Resistance of Sacrificial Plasma-Sprayed Mullite-YSZ Protective Layer on 8YSZ Thermal Barrier Coating, *Corros. Sci.*, 2020, **173**, p 108764.
13. S.H. Liu, C.X. Li, and H.Y. Zhang, A Novel Structure of YSZ Coatings by Atmospheric Laminar Plasma Spraying Technology, *Scr. Mater.*, 2018, **153**, p 73–76.
14. G. Mauer, M.O. Jarligo, D.E. Mack, and R. Vaßen, Plasma-Sprayed Thermal Barrier Coatings: New Materials, Processing Issues, and Solutions, *J. Therm. Spray. Techn.*, 2013, **22**(5), p 646–658.
15. S.H. Liu, J.P. Trelles, and A.B. Murphy, Low-Pressure Plasma-Induced Physical Vapor Deposition of Advanced Thermal Barrier Coatings: Microstructures, Modelling and Mechanisms, *Mater. Today Phys.*, 2021, **21**, p 100481.
16. S. Lakiza, O. Fabrichnay, C.H. Wang, M. Zinkevich, and Aldinger, Phase Diagram of the ZrO_2-Gd_2O_3-Al_2O_3 System, *J. Eur. Ceram. Soc.*, 2006, **26**(3), p 233–246.
17. R. Vaßen, A. Stuke, and D. Stöver, Recent Developments in the field of Thermal Barrier Coatings, *J. Therm. Spray. Techn.*, 2009, **18**(2), p 181–186.
18. S. Kramer, J. Yang, and C.G. Levi, Infiltration-Inhibiting Reaction of Gadolinium Zirconate Thermal Barrier Coatings with CMAS Melts, *J. Am. Ceram. Soc.*, 2008, **91**(2), p 576–583.
19. G. Dwivedi, V. Viswanathan, S. Sampath, A. Shyam, E. Lara-Curzio, and K. Faber, Fracture Toughness of Plasma-Sprayed Thermal Barrier Ceramics: Influence of Processing, Microstructure, and Thermal Aging, *J. Am. Ceram. Soc.*, 2014, **97**(9), p 2736–2744.
20. R. Vaßen, X. Cao, F. Tietz, and D. Basu, Zirconates as New Materials for Thermal Barrier Coatings, *J. Am. Ceram. Soc.*, 2000, **83**(8), p 2023–2028.
21. Y.J. Su, R.W. Trice, K.T. Faber, H. Wang, and W.D. Porter, Thermal Conductivity, Phase Stability, and Oxidation Resistance of $Y_3Al_5O_{12}$(YAG)/Y_2O_3-ZrO_2(YSZ) Thermal-Barrier Coatings, *Oxid. Met.*, 2004, **61**, p 253–271.
22. S.W. Jung, S. Park, and D. Choi, Efficient Drug Delivery Carrier Surface without Unwanted Adsorption Using Sulfobetaine Zwitterion, *Adv. Eng. Mater.*, 2020, **23**, p 2001433.
23. M. Gell, J. Wang, R. Kumar, J. Roth, and E.H. Jordan, Higher Temperature Thermal Barrier Coatings with the Combined Use of Yttrium Aluminum Garnet and the Solution Precursor Plasma Spray Process, *J. Therm. Spray. Techn.*, 2018, **27**(4), p 543–555.
24. G.R. Li, J.G. Yang, and C.X. Li, A Comprehensive Mechanism for the Sintering of Plasma-Sprayed Nanostructured Thermal Barrier Coatings, *Ceram. Int.*, 2017, **43**, p 9600–9615.
25. R. Kumar, E. Jordan, M. Gell, J. Roth, C. Jiang, J. Wang, and S. Rommel, CMAS Behavior of Yttrium Aluminum Garnet (YAG) and Yttria-Stabilized Zirconia (YSZ) Thermal Barrier Coatings, *Surf. Coat. Tech.*, 2017, **327**, p 126–138.
26. M.J. Liu, G. Zhang, Y.H. Lu, J.Q. Han, G.R. Li, C.X. Li, C.J. Li, and G.J. Yang, Plasma Spray-Physical Vapor Deposition toward Advanced Thermal Barrier Coatings: A Review, *Rare. Met.*, 2020, **39**(5), p 479–497.
27. R. Wellman, G. Whitman, and R.J. Nicholls, CMAS Corrosion of EB PVD TBCs: Identifying the Minimum Level to Initiate Damage, *Int. J. Refract. Met. H.*, 2010, **28**(1), p 124–132.
28. K. Stephan, J. Yang, and C.G. Levi, Thermo Mechanical Interaction of Thermal Barrier Coatings with Molten CaO-MgO-Al_2O_3-SiO_2 (CMAS) Deposits, *J. Am. Ceram. Soc.*, 2006, **89**(10), p 3167–3175.
29. Y. Kuru, O. Savasir, S.Z. Nergiz, C. Oncel, and P. Aken, Yttrium Aluminum Garnet as a Scavenger for Ca and Si, *J. Am. Ceram. Soc.*, 2008, **91**(11), p 3663–3667.